# Direct detection of induced magnetic moment and efficient spin-to-charge conversion in graphene/ferromagnetic structures

J. B. S. Mendes,[1,*] O. Alves Santos,[1,2] T. Chagas,[3] R. Magalhães-Paniago,[3] T. J. A. Mori,[4] J. Holanda,[2] L. M. Meireles,[3] R. G. Lacerda,[3] A. Azevedo,[2] and S. M. Rezende[2]

[1]*Departamento de Física, Universidade Federal de Viçosa, 36570-900 Viçosa, Minas Gerais, Brazil*
[2]*Departamento de Física, Universidade Federal de Pernambuco, 50670-901 Recife, Pernambuco, Brazil*
[3]*Departamento de Física, Universidade Federal de Minas Gerais, 31270-901 Belo Horizonte, Minas Gerais, Brazil*
[4]*Laboratório Nacional de Luz Síncrotron, Centro Nacional de Pesquisa em Energia e Materiais, 13083-970 Campinas, São Paulo, Brazil*

(Received 31 October 2018; revised manuscript received 27 March 2019; published 28 June 2019)

This article shows that the spin-to-charge current conversion in single-layer graphene (SLG) by means of the inverse Rashba-Edelstein effect (IREE) is made possible with the integration of this remarkable 2D material with the unique ferrimagnetic insulator yttrium iron garnet (YIG = $Y_3Fe_5O_{12}$) as well as with the ferromagnetic metal permalloy (Py = $Ni_{81}Fe_{19}$). By means of x-ray absorption spectroscopy and magnetic circular dichroism techniques, we show an induced magnetic moment in carbon atoms of the SLG due to the proximity effect with the magnetic layer. The spin currents are generated in the magnetic layer by spin pumping from microwave-driven ferromagnetic resonance and are detected by a dc voltage along the graphene layer, at room temperature. The spin-to-charge current conversion, occurring at the graphene layer, is explained by the extrinsic spin-orbit interaction induced by the proximity effect with the ferromagnetic layer. The results obtained for the SLG/YIG and SLG/Py systems confirm very similar values for the IREE parameter, which are larger than the values reported in previous studies for SLG. We also report systematic investigations of the electronic and magnetic properties of SLG/YIG by means of scanning tunneling microscopy.

DOI: 10.1103/PhysRevB.99.214446

## I. INTRODUCTION

New phenomena discovered in condensed matter physics and materials science in the last decades have shown that spintronics has many advantages over conventional electronics, and several spin-based devices are being used in consumer electronics [1,2]. Nowadays, generation, transport, and manipulation of spin currents—i.e., net flows of spin angular momentum—are among the main challenging topics in this research area. In turn, among the main phenomena to generate and manipulate spin currents, one can mention the spin-pumping effect (SPE), the spin Hall effect (SHE), and its Onsager reciprocal, the inverse SHE (ISHE) [3–11]. In the SPE, the precessing magnetization in a ferromagnetic material (FM) generates a pure spin current in an adjacent normal metal (NM), and in the SHE, an unpolarized charge current is partially converted into a transverse spin current by the spin-orbit coupling (SOC). Spin current has the advantage of flowing in both metallic and insulating materials that can be magnetic or nonmagnetic. These features increase the range of spintronics phenomena that are of interest for basic and applied research, such as (i) spin transport in magnetic insulators and organics materials [12–17]; (ii) spin-to-charge current conversion in paramagnetic, ferromagnetic, and antiferromagnetic metals, as well as in semiconductors [18–28]; (iii) magnetization manipulation by spin transfer torque (STT) [29–33]; and spin-charge interplay in two-dimensional systems based on the Rashba-Edelstein effect [34–41].

From the applications point of view the creation of spin-logic devices, which allow the control and transport of the spin current over long distances, is one of the major research challenges in spintronics. In this regard, graphene—a single atomic layer of carbon atoms in a honeycomb lattice [see Fig. 1(c)]—has attracted great attention as a promising material for spin-based devices due to its exceptional electronic transport properties, excellent charge carrier mobility, quantum transport, long spin diffusion lengths, and spin relaxation times [42–46]. However, due to the low atomic number of carbon, the Dirac electrons in intrinsic graphene have a weak SOC and no magnetic moments, thus reducing the promise of applications in spintronics [2]. In order to overcome this limitation, several mechanisms and structures have been proposed mainly focused on the improvement of local magnetic moments and spin-orbit coupling in graphene. Among them we may cite (i) functionalization of graphene with small doses of adatoms or nanoparticles [45,46]; (ii) development of nanostructures with gate electrodes of ferromagnetic materials [47,48]; and (iii) directly attaching graphene in contact with a ferromagnetic insulator (FMI) or a ferromagnetic metal (FM), to induce magnetic proximity effects [38,49–53]. More recently, a large enhancement of the SOC has been shown in graphene when it is directly fabricated on top of semiconducting transition-metal dichalcogenides [54–57].

Recent experimental studies have shown that yttrium iron garnet (YIG = $Y_3Fe_5O_{12}$) turned out to be an ideal FMI

*Corresponding author: joaquim.mendes@ufv.br

 ©2019 American Physical Society

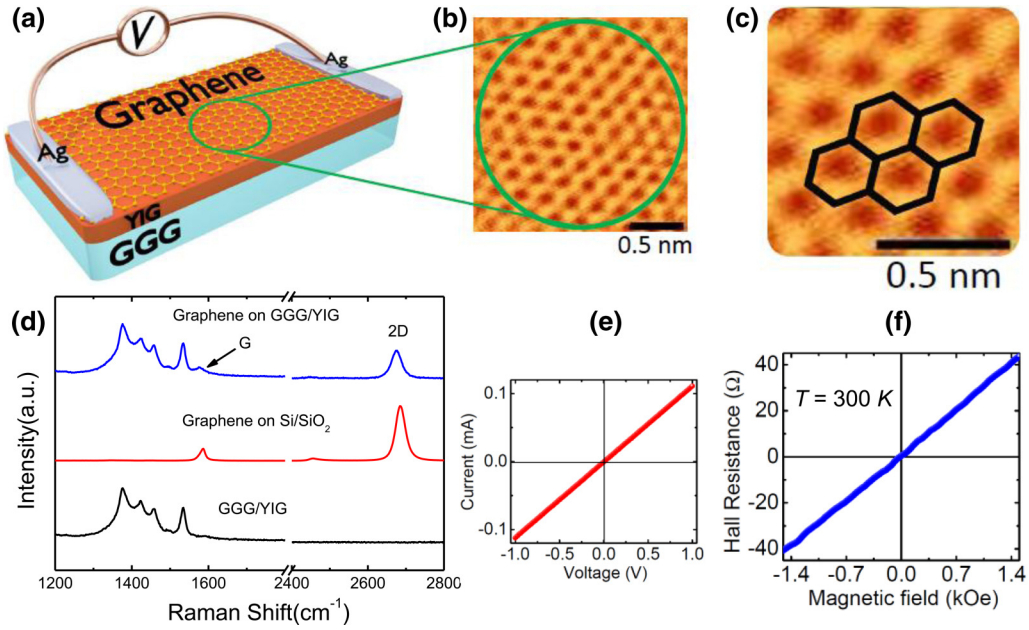


FIG. 1. (a) Sketch showing the YIG/graphene structures and the electrodes used to measure the dc voltage due to the IREE charge current in the graphene layer resulting from the spin currents generated by microwave FMR spin pumping. (b) STM image showing the surface details from an arbitrary region in the SLG/YIG sample. (c) High-resolution image showing the typical hexagons of the graphene deposited on YIG. (d) Raman spectroscopy spectra of GGG/YIG, $SiO_2$/graphene, and GGG/YIG/graphene. (e) *I-V* curve of the YIG/SLG structure demonstrating the formation of Ohmic contacts between the electrodes and the SLG. (f) Low-magnetic-field dependence of the Hall resistance at room temperature.

material to induce spin properties in hybrid structures with single-layer graphene (SLG) [38,58–62]. Among other reasons for the use of YIG, we can mention its excellent mechanical and structural properties, as well as its extraordinary low magnetic damping. At the same time, the metallic ferromagnetic permalloy (Py = $Ni_{81}Fe_{19}$) can be used instead of YIG if a conducting material is required for device development. In this paper, we report an extensive investigation of spin-current to charge-current conversion by the inverse Rashba-Edelstein effect (IREE) in large-area SLG grown by chemical vapor deposition (CVD) on YIG and Py films. Thus, we show that SLG in atomic contact with both magnetic materials exhibits an appreciable extrinsic SOC that enhances the IREE. Besides that, as the unequivocal proof of the proximity-induced magnetism in graphene, we perform x-ray magnetic circular dichroism (XMCD) measurements in YIG/SLG and Py/SLG samples. The XMCD results confirm the existence of an induced magnetic moment at the carbon atoms of graphene.

## II. SAMPLE PREPARATION AND CHARACTERIZATION

In the experiments reported here, we have investigated two types of heterostructures. In the first structure, the graphene is interfaced with a ferrimagnetic insulator material (sample A: YIG/SLG), and in the second heterostructure, the graphene is interfaced with a conductive ferromagnetic material (sample B: Py/SLG). As the ferrimagnetic insulator material we have used a single-crystal YIG film with thickness 6.0 $\mu$m grown by liquid-phase epitaxy on a 0.5-mm-thick substrate of (111) gadolinium gallium garnet (GGG). The YIG samples were cut from the same GGG/YIG wafer in the form of rectangles with lateral dimensions $2.5 \times 8.0$ mm$^2$. The samples were prepared in the following way. The graphene layers were grown on Cu foils inside a CVD chamber at 1000 °C with a mixture of $CH_4$ (33% volume) and $H_2$ (66% volume) at 330 mTorr for 2.5 hours [63,64]. A 120-nm-thick layer of PMMA is spun on top of the graphene/Cu surface and then the Cu is etched away. The PMMA/graphene structure is now transferred to the YIG film. Finally, the PMMA is removed using solvents and the sample receives two silver paint contacts as illustrated in Fig. 1(a) [see Appendix A and Fig. 8 for further details on the growth conditions as well as the transference of graphene]. For sample B preparation, we followed the same procedure, but in this case the graphene is transferred directly to the substrate of $SiO_2$(300 nm)/Si(100). As schematically shown in Fig. 6(a), the SLG surface is partially covered by a Py layer deposited by dc sputtering and leaving the ends free to coat two Ag electrodes. With this configuration, the effect of the Py conductivity does not affect the electrical detection of the spin-current to charge-current conversion that occurs on the SLG. The scanning tunneling microscopy (STM) image of Fig. 1(b) shows surface details for the SLG/YIG sample, where it allows us to observe the flat and homogeneous graphene surface. The honeycomb hexagon lattice of the SLG, deposited onto YIG, is clearly seen in the high-resolution STM image shown in Fig. 1(c).

Figure 1(d) shows the Raman spectroscopy spectra of GGG/YIG, $SiO_2$/SLG, and GGG/YIG/SLG. The spectrum at the top of Fig. 1(d) shows the lines of GGG/YIG/SLG. The characteristic peaks from the G (1580 cm$^{-1}$) and 2D (2700 cm$^{-1}$) bands of the SLG confirm the successful transfer of graphene to the surface of the YIG layer. Figure 1(e) shows the measured linear *I-V* characteristics, indicating Ohmic contacts between the Ag electrodes and the graphene. The

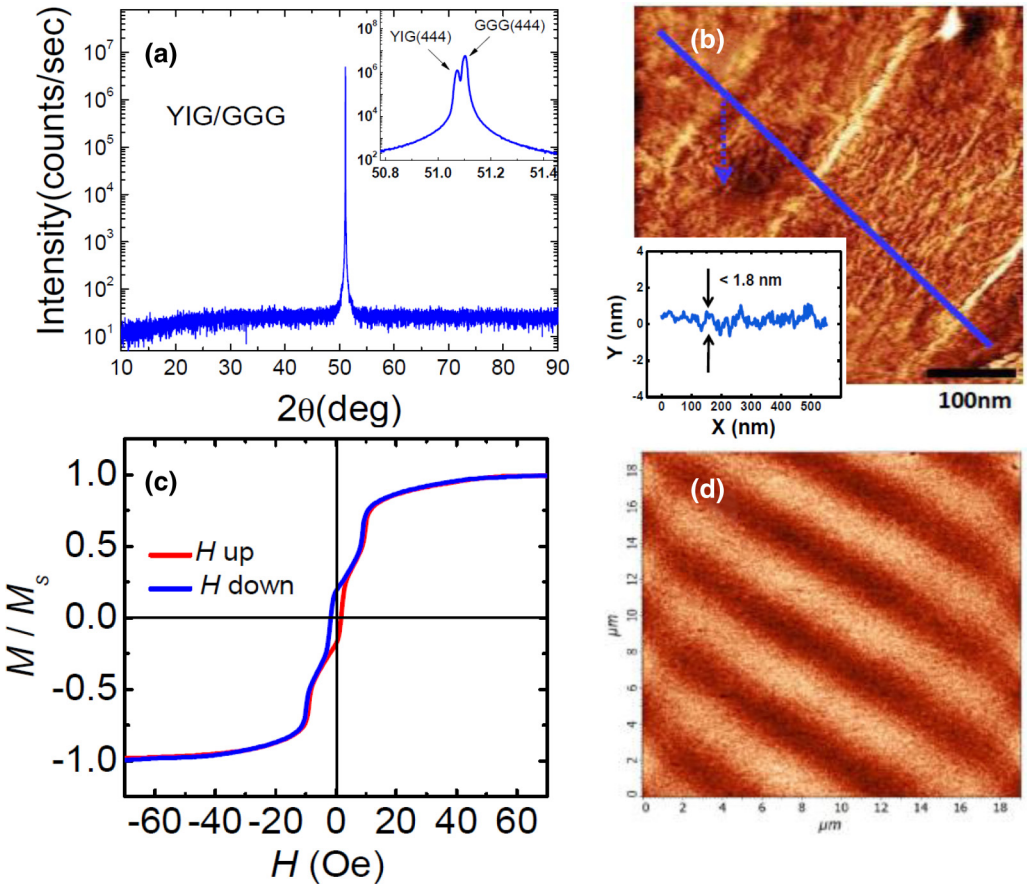


FIG. 2. (a) Out-of-plane XRD patterns ($\omega$-$2\theta$ scans) of YIG film grown on GGG substrate. The XRD spectrum detailing the position of the peaks of the YIG film and the GGG substrate is shown in the inset. (b) AFM image of the YIG film surface. The line trace in (b) confirms that the YIG surface has a very small roughness. Panel (c) shows a VSM hysteresis curve for the YIG samples used in this work. (d) MFM image of the as-grown 6-$\mu$m-thick YIG film showing up- and down-oriented domains as regions of light and dark contrast.

magnetic field dependence of the Hall resistance can be seen in Fig. 1(f), in the field range in which the magnetization of YIG rotates out-of-plane.

Additional characterizations of the high-quality YIG layer used in this work can be verified in Fig. 2, such as x-ray diffraction measurements, surface roughness, and magnetic hysteresis, as well as the magnetic domain structures measured by means of the magnetic force microscopy (MFM) technique. The crystallographic structure of the YIG was assessed by x-ray diffraction (XRD) measurements. The XRD patterns were recorded using the Bruker D8 Discover Diffractometer equipped with Cu $K\alpha$ radiation ($\lambda = 1.5418$Å). The out-of-plane XRD pattern is shown in Fig. 2(a). The diffraction patterns were obtained at angles between 10° and 90° ($2\theta$). Only the line associated with the (444) crystal plane of YIG appears in the out-of-plane XRD pattern, indicating that unexpected phases were not detected. The XRD spectrum at high resolution detailing the position of the peaks of the YIG film and the GGG substrate is shown in the inset. The results of the XRD measurements indicate that the present YIG film is epitaxially grown on the GGG substrate. Figure 2(b) shows an atomic force microscopy (AFM) image of the YIG film surface. The line trace in Fig. 2(b) confirms the uniformity of the YIG film surface with very small roughness. Figure 2(c) shows a magnetization hysteresis curve for a representative YIG sample measured by a VSM (vibrating sample magnetometer). The data show a small hysteresis, with a coercive field of 1.8 Oe and remanent magnetization of 0.12 of the saturation value. Figure 2(d) shows a magnetic force microscopy image for the demagnetized state in the 6-$\mu$m-thick YIG film, which exhibits a typical stripe domain structure. All additional measurements were obtained at room temperature.

## III. STM/STS EXPERIMENTS

Scanning tunneling microscopy/spectroscopy (STM/STS) measurements were carried out using a Nanosurf microscope (in constant-current mode) operating at room temperature (300 K) using freshly cleaved Pt-Ir tips. Spectroscopy data were obtained through numerical differentiation of measurements of the tunneling current as a function of the sample bias at selected points (averaged over ten individual STS measurements). The STM images were obtained employing a voltage of 40.0 mV to 70.0 mV and a tunneling current of 1.0 nA to 1.5 nA. In order to investigate the electronic response of the sample under the application of a magnetic field ($H$), STM/STS measurements were carried out in atomically flat regions as well as in the vicinity of steps and edges. These are regions where the spin orientation of the electrons

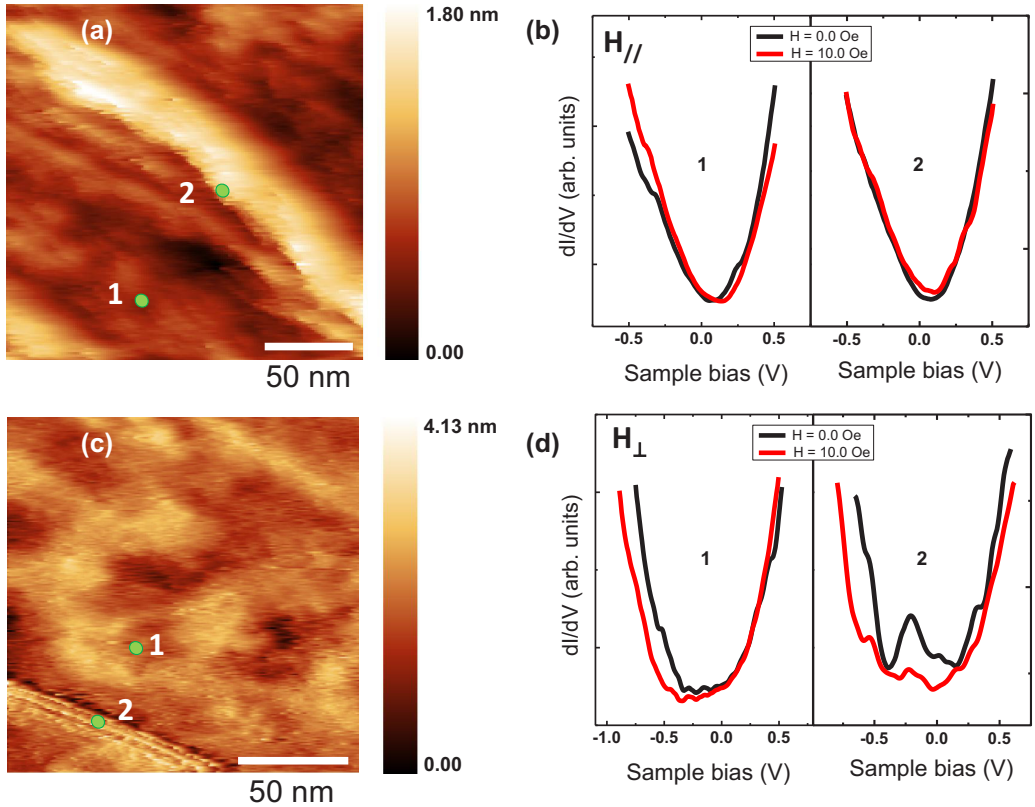


FIG. 3. (a) STM topography image of the graphene/YIG sample showing a region of low roughness. (b) STS spectra acquired at the points marked with the green circles [shown in (a)] and labeled as 1 (left panel) and 2 (right panel). The black curves were measured in the absence of a magnetic field and the red curves were measured for a magnetic field of 10.0 Oe parallel to the sample surface. (c) STM image showing an atomically flat region with some steps in the left lower corner. (d) STS spectra acquired at the points marked with the green circles [shown in (c)] and labeled as 1 (left panel) and 2 (right panel). The black curves were measured in the absence of a magnetic field and the red curves were measured for a magnetic field of 10.0 Oe perpendicular to the sample surface.

is changed due to the presence of a magnetic field [65]. An STM image of the sample, where one observes a region of low roughness with the presence of some steps, is shown in Fig. 3(a). STS spectra, Fig. 3(b), were measured at the points marked with the green circles in the STM image and labeled as 1 (left plot), i.e., at a flat region, and 2 (right plot), i.e., at a step edge. Both measurements were repeated with and without the presence of a magnetic field parallel to the sample surface. In this figure the black and the red curves, in both panels, are related to STS spectra measured for $H = 0.0$ Oe and $H = 10.0$ Oe, respectively. In both conditions a V-shaped spectrum, compatible with the typical electronic signature of monolayer graphene [44], is observed. In this measurement one also observes a natural broadening of $4K_BT \sim 100$ meV near the Dirac point, which is a consequence of temperature of the experiment (300 K) [66]. This result evidences that the graphene layer is decoupled from the substrate for this particular region since its local density of states (LDOS) is not significantly affected by the substrate.

On the contrary, for Figs. 3(c) and 3(d) a different scenario is observed. In Fig. 3(c) an atomically flat region with the presence of some steps is presented. Differently from the previous case, for this area of the system a magnetic field perpendicular to the sample surface was applied. STS spectra for points 1 (flat region) and 2 (step region) indicated in this figure are shown in Fig. 3(d), in the left and right panels, respectively. For the atomically flat region marked as 1, the STS spectra slightly differ from the ones shown in the left panel of Fig. 3(b). In this last case the STS spectra observed do not present a completely linear relationship between LDOS and energy, which indicates a higher degree of coupling of the graphene sheet to the substrate. In addition, no significant changes are observed due to the application of $H$. For the STS spectra acquired at point 2 [shown in the right panel of Fig. 3(d)] a distinct electronic behavior is noticed. Analyzing the LDOS measured at the step without the application of a magnetic field one observes a peak at $-0.25$ V, which may be consistent with the presence of edge states. Interestingly, this peak is highly suppressed in the presence of a magnetic field of 10.0 Oe showing that the LDOS is influenced by $H$ under this condition. This effect may be directly related to the change of the magnetoresistance for different values of magnetic fields reported in Ref. [38]. Thus, this result indicates that the changes observed in the magnetoresistance for $H = 0.0$ Oe and $H = 10.0$ Oe are possibly related to the local electronic density of edge states. All STS measurements presented in the current paper were acquired after at least 30 minutes of waiting time, i.e., after a time in which thermal drift is no longer significant so that the tip position is not highly affected by the temperature of the system in a short time. Measurements were performed with high reproducibility and the spatial resolution is below 1 nm. Further

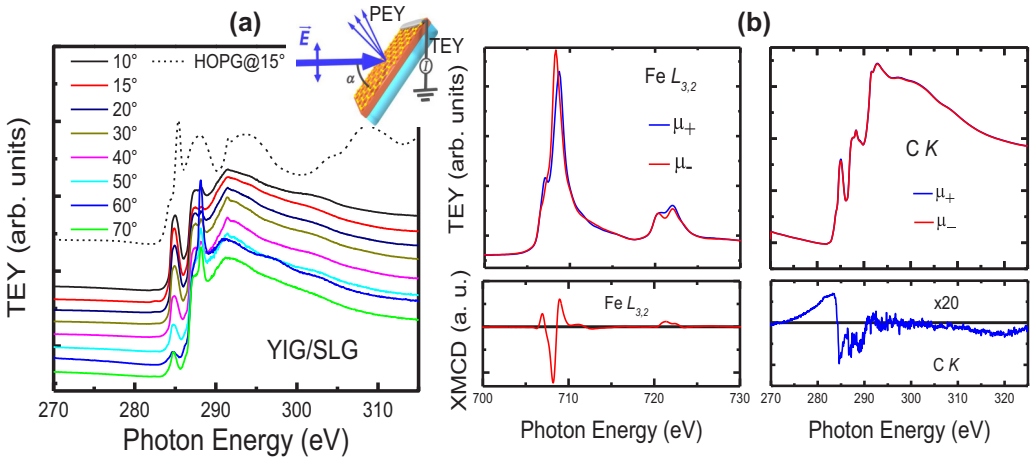


FIG. 4. (a) Spectra acquired around the carbon $K$ edge of the YIG/graphene, with the electric field vector of the linearly polarized beam pointing along the vertical direction, for several incidence angles $\alpha$. The dash-lined spectrum is acquired from a HOPG reference sample with an incidence angle of 15°. (b) XAS spectra acquired around the Fe $L_{3,2}$ (left) and C $K$ (right) edges, for both right- and left-handed circular polarizations of the light, under an applied magnetic field of 300 Oe and at an incidence angle of 15°. The bottom of the figure presents the XMCD asymmetries.

discussion of the STM/STS measurements can be found in Appendix E.

## IV. XAS AND XMCD EXPERIMENTS

Electronic orbital orientation and element-specific magnetic characterization were performed with x-ray absorption spectroscopy (XAS), i.e., x-ray linear (XLD) and magnetic circular dichroism (XMCD), respectively. The measurements were carried out at the U11A-PGM beamline of the Brazilian Synchrotron Light Laboratory (LNLS), near both the carbon $K$ and the iron $L_{3,2}$ absorption edges, at room temperature in total electron yield (TEY) mode. In order to determine the average spatial orientation of the molecular orbitals ($\pi$ or $\sigma$) at the YIG/SLG interface, several XAS spectra were acquired by keeping the electric field of the linearly polarized light pointing along the vertical direction while the sample was tilted so that the angle between the electric field and the surface normal was varied from 10° to 90° [see inset of Fig. 4(a) for details on the geometry]. To check the magnetism at both carbon and iron absorption edges, the XAS spectra were collected under four configurations of applied magnetic field and polarization of light (±300 Oe and right/left-handed circular polarization), with a grazing incidence angle of 15°. Although it is faster to change polarization than magnetic field at the end station/beamline utilized for the experiment, the x-ray natural circular dichroism (XNCD) due to the chirality of layered graphene [67] that may arise locally from small imperfections of the graphene layer under the large area illuminated by the beam requires the inversion of the magnetic field to get rid of the contribution of the XNCD to the circular dichroism. Therefore, in order to get the best quality data, the XMCD asymmetry spectra were obtained by taking the average of the differences (modulus) between the spectra acquired for two different polarizations for each magnetic field direction [$\mathrm{XMCD} = (|\mathrm{TEY}_{H_+,\mu_+} - \mathrm{TEY}_{H_+,\mu_-}| + |\mathrm{TEY}_{H_-,\mu_+} - \mathrm{TEY}_{H_-,\mu_-}|)/2$, where $\mathrm{H}_+/\mathrm{H}_-$ and $\mu_+/\mu_-$ stand for the direction of the magnetic field and for the handedness of the circular polarization, respectively].

The average spatial orientation of the molecular orbitals at the YIG/SLG interface can be addressed by acquiring several x-ray absorption spectra for different orientations of the sample out-of-plane direction with respect to the electric field direction of the linearly polarized x-ray beam. In this experiment, the absorption intensity of a specific orbital final state presents a maximum if the electric field is parallel to the direction of maximum density of states of the molecular orbital [68]. On the other hand, the absorption intensity vanishes if the electric field is perpendicular to the molecular orbital axis. Figure 4(a) presents spectra acquired near the carbon $K$ edge, with the electric field vector of the linearly polarized beam pointing along the vertical direction, for several incidence angles $\alpha$. In the geometry illustrated in the inset of the figure, the electric field of the light is along the surface normal at $\alpha = 0°$, and parallel to the surface at $\alpha = 90°$. The changes of the XAS line shape show that the spectral feature around 285 eV, which is assigned to the C $1s \rightarrow \pi^*$ transition of $1s$ core electrons into unoccupied $\pi^*$ states, is remarkably strong for grazing incidence angles and tends to vanish as the incidence angle is increased towards normal incidence. This strong angular dependence of the XAS line shape is due to different orbital orientations and demonstrates that the $\pi^*$ unoccupied states are aligned out-of-plane, as is expected for the C $p_z$ orbitals in the graphene-type layered $sp^2$ coordination. This agrees with the structural characterization by STM and also proves the good quality of the SLG.

It is worth noting the spectral feature around 286–290 eV, which is ascribed to the PMMA presence on the sample surface (residue of the graphene transferring process) and jeopardizes the analysis of the spectra as it is in the very middle region between the spectral features due to C $1s \rightarrow \pi^*$ (283–289 eV) and C $1s \rightarrow \sigma^*$ (289–315 eV) transitions. A comparison with a spectrum around the C $K$ edge of highly oriented pyrolytic graphite [dash-lined spectrum in Fig. 4(a), acquired from a HOPG sample with an incidence angle of 15°]

allows one to notice changes in the line shape of the YIG/SLG spectrum. These changes were attributed to chemisorption as suggested in previous work [69,70]. Small shifts in energy and remarkable broadening of the $\pi^*$ and $\sigma^*$ resonances suggest orbital hybridization and electron sharing along the interface, with delocalization of the corresponding core-excited state. Such a covalent interfacial bonding between carbon atoms in the SLG and iron atoms in the YIG could be the origin of the magnetic proximity effect detected in carbon atoms. In a way very similar to what has been demonstrated for the system Ni(111)/graphene [69,70], we suggest that a hybridization between graphene $\pi$ and valence-band states at the YIG/graphene interface leads to partial charge transfer of spin-polarized electrons from the substrate to C atoms in graphene. In this sense, the XMCD suggests an induced magnetic moment of carbon atoms, as shown in Fig. 4(b).

Figure 4(b) shows XAS spectra acquired around the Fe $L_{3,2}$ (left) and C $K$ (right) edges, for both right- and left-hand circular polarizations of light, under an applied magnetic field of 300 Oe and at an incidence angle of 15°. The bottom of the figure presents the XMCD asymmetries, which were evaluated by taking the averaged difference between the difference of the spectra taken with two different polarizations under 300 Oe (shown in the figure) and the difference of the spectra taken under −300 Oe (not shown), as explained previously in this section. The Fe $L_{3,2}$ XAS/XMCD spectrum is in agreement with published spectroscopic data of iron (III) coordinated as it is in YIG [71]. Besides, the XAS experiments at the C $K$ absorption edge also indicate a finite dichroic signal. Here it is important to point out that the line shape of the difference spectra at this absorption edge is a little distorted due to experimental problems that make the normalization and background subtraction of the data set a challenge, and consequently the magnitude of the XMCD asymmetry very close to the detection limit of the experiment. These problems are discussed in Appendix C. Despite the presence of the PMMA feature in the XAS spectra, the XMCD spectrum has the maximum asymmetry at the $1s \rightarrow \pi^*$ resonance. In other words, the major magnetic response of the carbon atoms seems to arise from transitions of the $1s$ electrons into the unoccupied $\pi^*$ states, the transitions to the $\sigma^*$ states yielding a very weak magnetic signal. This result, also in accordance with Refs. [69,70] for Ni(111)/graphene, suggests that mostly the C $2p_z$ orbitals of the SLG are magnetically polarized due to the hybridization with the valence-band states of the YIG substrate. In Ref. [72] the authors report on magnetic signals of carbon observed by the x-ray resonant magnetic reflectivity technique, the ferromagnetism of carbon in the Fe/C multilayered system being related to the hybridization between the Fe $3d$ band and the C $p_z$ orbitals. Besides, there are other reports on magnetism in the Fe/C interface investigated by XMCD and on the magnetism induced in carbon nanotubes on ferromagnetic Co substrate due to spin-polarized charge transfer at the interface [73,74].

The XAS and XMCD spectra of a sample Py/SLG were also acquired (see Fig. 9 in Appendix B). Similarly to the results obtained for the sample YIG/SLG, the XAS spectra for the Py/SLG, measured with linear polarization and varying the incidence angle, confirm the good quality of that sample, with the $\pi^*$ unoccupied states of carbon pointing out-of-plane. In its turn, the circular dichroism measured at the carbon $K$ edge also present an asymmetry around the feature related to the $\pi^*$ unoccupied states. Combined with the XMCD spectra at the Ni $L_{3,2}$ edge, the results also suggest that the C $2p_z$ orbitals of the SLG are magnetically polarized due to the hybridization with the valence-band states of the adjacent Py layer.

## V. SPIN-PUMPING EXPERIMENTS

In the spin-pumping experiments, the FM/SLG bilayer sample is under action of a small radio-frequency (rf) magnetic field applied perpendicularly to a dc magnetic field in the ferromagnetic resonance (FMR) configuration. The precessing magnetization $\vec{M}$ in the FM layer generates a spin-current density at the FM/SLG interface, $\vec{J}_S = (\hbar g_{\rm eff}^{\uparrow\downarrow}/4\pi M^2)(\vec{M} \times \frac{\partial \vec{M}}{\partial t})$, where $g_{\rm eff}^{\uparrow\downarrow}$ is the real part of the effective spin-mixing conductance at the interface that takes into account the spin-pumped and backflow spin currents [6]. The net spin current that flows into the adjacent conducting layer produces two effects: (i) it increases the damping of the magnetization due to the flow of spin angular momentum out to the adjacent material; (ii) due to the inverse Rashba Edelstein effect (IREE), the spin current that flows out of the FM layer is converted into a perpendicular charge current that produces a dc voltage at the ends of the graphene layer, measured between the two Ag electrodes. By investigating these two independent phenomena it is possible to extract material parameters from the measurements of the FMR absorption and the spin-pumping voltage.

In the microwave FMR absorption and spin-charge conversion experiments the sample with electrodes, shown in Figs. 1(a) and 6(a), is mounted on the tip of a PVC rod and inserted into a small hole in the back wall of a rectangular microwave cavity operating in the transverse electric $TE_{102}$ mode, in a nodal position of maximum-rf magnetic field and zero electric field. The sample is introduced through a small hole in the back wall of a rectangular microwave waveguide in a position of maximum microwave field $h$ and zero-rf electric field. This precaution avoids the generation of galvanic effects in the magnetic layer driven by the rf electric field. The waveguide is placed between the poles of an electromagnet so that the sample can be rotated while maintaining the static and rf fields in the sample plane and perpendicular to each other. With this configuration we can investigate the angular dependence of the FMR absorption spectra. For sample A, we use a shortened waveguide instead of a resonating microwave cavity to avoid detuning produced by the strong resonance of YIG and also nonlinear effects. Field scan spectra of the derivative $dP/dH$ of the microwave absorption are obtained by modulating the dc field with a weak ac field at 1.2 kHz that is used as the reference for lock-in detection. Figures 5(b) and 6(b) show the derivative of the FMR spectra of the two samples investigated in this work. Both spectra were obtained with $H$ in-plane and normal to the long sample dimension, frequency $f = 9.4$ GHz, and input microwave power of 80 mW for sample A and 24 mW for sample B. In Fig. 5(a), for a bare YIG film, one clearly sees the various lines corresponding to standing spin-wave modes with quantized wave numbers $k$ due to the boundary conditions

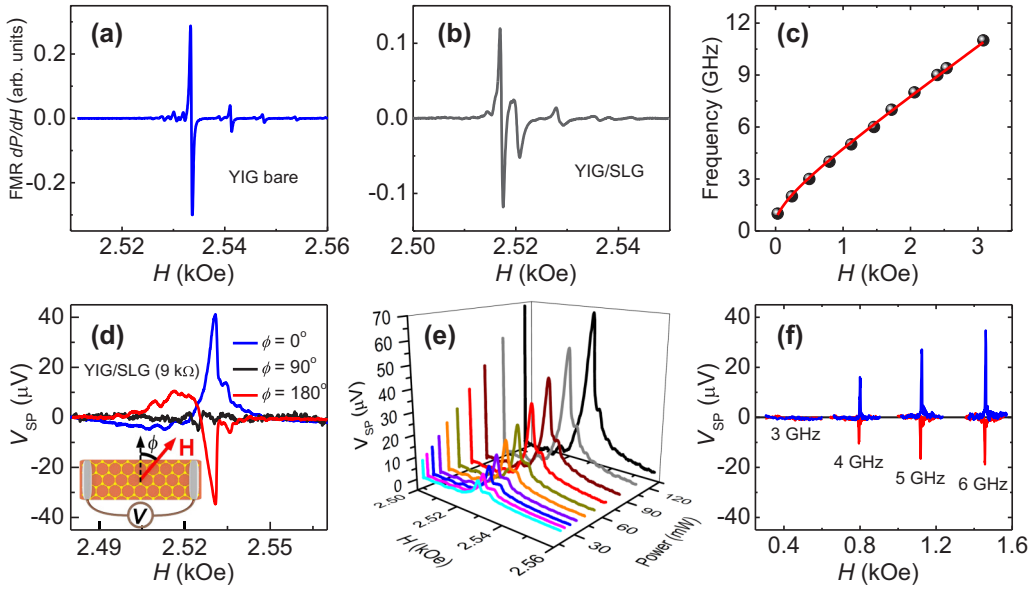


FIG. 5. Panels (a) and (b) show the field scan FMR microwave absorption derivative spectra for YIG and YIG/SLG, respectively, where the magnetic field is applied in the film plane, transversally to the long dimension. (c) Driving frequency versus FMR resonance field, where the solid red line corresponds to the best fit of the Kittel equation. (d) Field scan of dc spin-pumping voltage measured with 9.4 GHz microwave driving with power of 80 mW in YIG/SLG for three different directions between in-plane magnetic field and detection electrodes. (e) Field scan of dc SPE voltage for different input microwave power. The results show the linear variation of the peak voltage with microwave power in YIG/SLG. (f) SPE voltage for four different driving microwave frequencies for $\phi = 0°, 180°$.

at the edges of the film. The strongest line corresponds to the uniform (FMR) mode that has frequency close to the spin-wave mode with $k = 0$, the lines to the left of the FMR correspond to hybridized standing spin-wave surface modes, whereas those to the right are volume modes. All modes have similar peak-to-peak linewidth of 0.39 Oe, corresponding to a half-width at half-maximum (HWHM) of $\Delta H \approx 0.34$ Oe of direct microwave absorption. Figure 5(b) shows the FMR absorption for the YIG/SLG sample. Due to the spin injection into graphene the linewidth of YIG/SLG increases up to $\Delta H_{\mathrm{YIG/LSG}} = 0.90$ Oe. As can be seen in Fig. 5(b), the contact of the YIG film with the graphene layer increases the FMR linewidth of YIG. From the line broadening we can obtain a good estimate for the spin-mixing conductance $g_{\mathrm{eff}}^{\uparrow\downarrow}$, using the relation $g_{\mathrm{eff}}^{\uparrow\downarrow} = \frac{4\pi M_S t_{\mathrm{FM}}}{\hbar\omega}(\Delta H_{\mathrm{FM/SLG}} - \Delta H_{\mathrm{FM}})$, from which we obtain $g_{\mathrm{eff}}^{\uparrow\downarrow} \approx 10^{14}\ \mathrm{cm}^{-2}$ from the YIG/SLG interface.

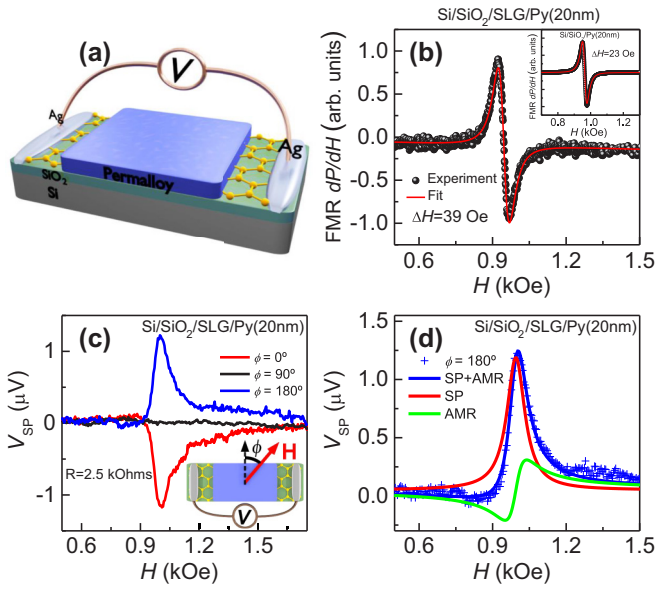


FIG. 6. (a) Sketch showing the $Si/SiO_2/SLG/Py(20\ nm)$ structure. (b) Field scan of derivative power absorption of $Si/SiO_2/SLG/Py(20\ nm)$. The best fit was adjusted with linewidth of 39 Oe, and the inset shows FMR absorption of Py on top of Si with $\Delta H = 23$ Oe. (c) The dc spin pumping voltage in SLG/Py. (d) The blue line represents a sum of the Lorentzian (symmetric red line) and the Lorentzian derivate (antisymmetric green line) best-fit form data of $V_{\mathrm{SP}}(\phi = 180°)$.

Figure 5(c) shows the FMR measurements carried at several microwave frequencies employing an FMR broadband spectrometer. The microwave excitation was carried out by means of a microstrip transmission line of copper, 0.5 mm wide and characteristic impedance $Z_0 = 50\ \Omega$, that was fabricated on a Duroid substrate, where the return is the ground plane on the back side of the board. The YIG film placed on top of the microstrip line separated by a 60-$\mu$m-thick Mylar sheet is excited by the rf magnetic field perpendicular to the static field $H$ applied in the film plane. By keeping the frequency value fixed and sweeping the static magnetic field, the variation of the transmitted power due to the FMR absorption is detected by a Schottky diode. The applied magnetic field is modulated with frequency 8.7 kHz and amplitude 0.45 Oe so as to allow lock-in detection of the field derivative of the power absorption. The solid red line in Fig. 5(c) was obtained from the fit with the Kittel equation, $f = \gamma[(H_R - H_A)(H_R + H_A + 4\pi M_S)]^{1/2}$, where $\gamma = g\mu_B/\hbar$ ($\approx 2.8$ GHz/kOe) is the gyromagnetic ratio, $g$ is

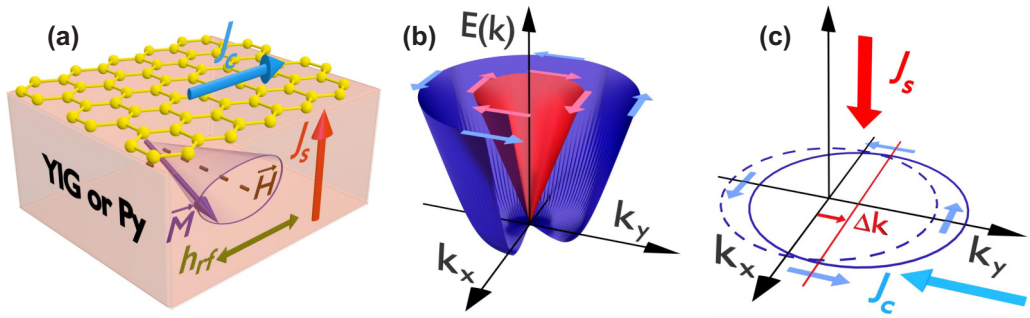


FIG. 7. (a) Schematic of the spin-to-charge conversion by the inverse Edelstein effect in FMR spin-pumping experiments on the graphene. (b) The spin-polarized band structure (electron energy $E$ as a function of in-plane momentum $k$) of 2D electron states at a Rashba interface. (c) The unbalanced spin states resulting from the 3D spin current creates a 2D charge current in the contour of the Rashba interface, i.e., inverse Edelstein effect.

the spectroscopic splitting factor, $\mu_B$ the Bohr magneton, $\hbar$ the reduced Planck constant, $H_A$ the in-plane anisotropy field, and $4\pi M_S = 1760$ G the saturation magnetization of YIG. With the fit shown in Fig. 5(c) we obtained $H_A = 28$ Oe.

The net spin current that reaches the YIG/SLG interface creates a spin accumulation on SLG; this accumulation can be converted into charge current. We can write the dc spin-pumping spin-current density at the YIG/SLG interface generated by magnetization precession as

$$J_S(0) = \frac{\hbar\omega p g_{\rm eff}^{\uparrow\downarrow}}{16\pi}\left(\frac{h_{\rm rf}}{\Delta H}\right)^2 L(H - H_R), \tag{1}$$

where $\Delta H$ and $H_R$ are the linewidth and field for resonance of the YIG/SLG bilayer, $L(H - H_R)$ represents the Lorentzian function, $p$ is the precession ellipticity, and $\omega = 2\pi f$ and $h_{\rm rf}$ are the frequency and amplitude of the driving microwave magnetic field, respectively [18]. This spin current is converted into a transversal charge current at the SLG by means of the IREE, which can be detected by measuring a dc voltage that sets up between the two Ag electrodes. The dc voltage is measured by a nanovoltmeter directly connected to the edges of sample as sketched in Figs. 1(a) and 6(a). The direct measurement of the spin-pumping voltage $V_{\rm SP}(H)$ spectra are obtained by sweeping the dc magnetic field with no ac field modulation. By rotating the sample in the plane, we measured the angular dependence of the voltage as a function of the angle $\phi$ [see inset of Fig. 5(d)]. Figure 5(d) shows the spectra of $V_{\rm SP}(H)$ obtained with microwave frequency $f = 9.4$ GHz and incident power 80 mW, for three field directions, $\phi = 0°, 90°, 180°$. The spectra exhibit a large peak at the FMR field position and lateral small peaks corresponding to the standing spin-wave modes. Moreover, this intensity is proportional to pumped spin current; the signal reverses at 180° and falls to noise level at 90°. It is important to mention that the voltage measured in Fig. 5(d) with microwave power of 80 mW is almost one order of magnitude greater than the values reported in Ref. [38], where an rf power of 150 mW was applied. The asymmetry between the positive and negative peaks is similar to that observed in other bilayer systems and can be attributed to a thermoelectric effect [75,76]. Figure 5(e) shows the field scan of spin-pumping voltage spectra for different input microwave power obtained for the $\phi = 0°$ configuration. Note that the amplitude of the peak voltage in YIG/SLG has a linear dependence with the microwave power, showing that nonlinear effects are not being excited in the power range of the experiments.

## VI. SPIN-TO-CHARGE CURRENT CONVERSION RESULTS

Figure 7(a) shows a schematic illustration of a spin-current generation driven by the spin-pumping effect, where the charge current $\vec{J}_C$ generated at the SLG is simultaneously orthogonal to the dc magnetic field $\vec{H}$ and to the spin current $\vec{J}_S$, for either YIG or Py. In systems such as YIG/SLG [38], Ag/Bi [34], and LAO/STO [35], the presence of two-dimensional SOC is driven by the Rashba effect [77], as illustrated in Fig. 7(b). This effect creates a spin split in the energy dispersion surfaces of the Rashba states, thus causing a locking between the momentum $k$ and the spin angular momentum of the electron. In this case, a 3D spin current overpopulates states on one side of the Fermi contour and depopulates states on the other, thereby creating a shift $\Delta k$ on the Fermi contours, which is equivalent to a charge current. This effect is called the inverse Rashba-Edelstein effect [34], as illustrated in Fig. 7(c), where a spin current ($-z$ direction) with spin polarization ($-x$ direction) creates a charge current ($-y$ direction). Using the relation [34] $j_C = (2e/\hbar)\lambda_{\rm IREE} J_S$, between the 3D spin current in Eq. (1) and 2D charge current in SLG we can estimate the $\lambda_{\rm IREE}$, which is a coefficient characterizing the IREE, with dimension of length and proportional to the Rashba coefficient, and consequently to the magnitude of the SOC in graphene. The charge current density produces a measured voltage described as $V_{\rm IREE} = R_S w j_C$. Using Eq. (1) one can express the IREE coefficient in terms of the measured voltage peak value by

$$\lambda_{\rm IEE} = \frac{4V_{\rm IREE}^{\rm peak}}{R_S w e f p g_{\rm eff}^{\uparrow\downarrow}(h_{\rm rf}/\Delta H)^2}, \tag{2}$$

where $R_S$ is the shunt resistance and $w$ is the width of SLG. Since YIG is insulating, here $R_S$ is the resistance of the graphene layer. Computing Eq. (2) with the parameters $V_{\rm IREE}^{\rm peak} = 40\ \mu$V, $R_S = 9$ k$\Omega$, $w = 3$ mm, $h_{\rm rf} = 3.5 \times 10^{-2}$ Oe, and $p = 0.3$, we obtain $\lambda_{\rm IREE} \approx 0.002$ nm, which is about twice the value measured for graphene reported in a previous

paper [38]. On the other hand, this value is about 2 orders of magnitude smaller than the one obtained for the Ag/Bi interface [34], and about one order of magnitude smaller than the one measured for the topological insulators [39,40]. Figure 5(f) shows the measurement of the spin-pumping voltage with scanning $H$ for several frequencies. Here, the amplitude of the spin-pumping voltage falls abruptly as the frequency decreases below 4 GHz. The reason is that for YIG films with thickness in the $\mu$m range [78] the three-magnon nonlinear process has the coincidence of frequencies that decreases the absorption abruptly at microwave power levels as low as 100 $\mu$W [79].

In a further investigation, we replaced the injector of spin current by a metallic ferromagnetic material. In this case, a layer of Py with 20 nm thickness was deposited on top of the SLG transferred on the Si/SiO(300 nm) substrate. Figure 6(a) shows the sketch of the heterostructure Si/SiO/SLG/Py with lateral dimensions of $3 \times 1.5$ mm. Once again, the sample was mounted on the tip of a PVC rod and inserted through a hole in the center of a back wall of a rectangular microwave cavity operating in the $TE_{102}$ mode, at a frequency of 9.4 GHz with a $Q$ factor of 2000. Figure 6(b) shows the FMR absorption, at 24 mW, for $SiO_2$/SLG/Py(20 nm). The FMR line shape was fitted with the derivative of a Lorentzian function, and the extracted FMR linewidth was 39 Oe. The inset of Fig. 6(b) shows the FMR absorption spectrum for an identical Py layer deposited on Si substrate, with a linewidth of $\Delta H_{\rm Py} = 23$ Oe. As occurred in YIG/SLG, the broadening of the FMR linewidth of Py in contact with the graphene layer produces an additional damping due to the spin pumping. We obtained $g_{\rm eff}^{\uparrow\downarrow} \approx 10^{15}$ cm$^{-2}$ for the SLG/Py interface, which is a value similar to the one observed in the Py/Pt interface [19,21,80]. The spin-pumping voltage shown in Fig. 6(c) was measured by exciting the FMR with the same microwave power. The scan field spectra exhibit the same feature as the $V_{\rm SP}$ measured in YIG/SLG, so that the voltage peak occurs at the FMR field value. However, the direction of spin injection into SLG/Py is opposite in comparison to YIG/SLG, once the ferromagnetic material is now on top of graphene. Therefore, an opposite spin-pumping voltage was measured for the same direction; i.e., the maximum positive value occurs for $\phi = 180^\circ$, negative for $\phi = 0^\circ$, and null value for $\phi = 90^\circ$. The field dependence voltage $V(H)$ in the case of Py can be adjusted by the sum of two components, as shown in Fig. 6(d), where the solid blue line of Fig. 6(c) was adjusted by $V(H) = V_{\rm sym}L(H - H_R) + V_{\rm asym}D(H - H_R)$. Here $L(H - H_R)$ is the (symmetric; solid red line) Lorentzian function and $D(H - H_R)$ is the (antisymmetric; solid green line) Lorentzian derivative centered about the FMR resonance field. The amplitude of the microwave field in Eq. (2) in Oe is related to the incident power, in W, by $h_{\rm rf} = 1.776(P_i)^{1/2}$. Taking into account the values $R_S = 2.5$ k$\Omega$, $w = 1.5$ mm, and the amplitude of symmetric component of $V(H)$, $V_{\rm sym} = V_{\rm IEE}^{\rm peak} = 1.14$ $\mu$V, we obtain $\lambda_{\rm IREE} \approx 0.003$ nm, which is similar to the previous value for YIG/SLG. The antisymmetric component $V_{\rm asym} = V_{\rm AMR} = 0.52$ $\mu$V is related to the contribution of the anisotropic magnetoresistance (AMR) that occurs on the Py and reflects on the edges of the graphene layer [18,81].

## VII. CONCLUSIONS

In this investigation we have demonstrated the optimal conversion of a spin current into a charge current in the large-area graphene deposited on YIG and Py films, which is attributed to the inverse Rashba-Edelstein effect (IREE). The results obtained for the SLG/YIG and SLG/Py systems confirm very similar values for the IREE parameter, which are larger than the reported values in the previous studies for SLG [38]. We believe that the spin-to-charge conversion efficiency can be attributed to the excellent structural and interface quality of SLG/FM heterostructures produced, which optimizes the transfer of spins. We have also shown that the carbon atoms of single layers of graphene acquire an induced magnetic moment due to the proximity effect with ferromagnetic surfaces. This result was confirmed by means of x-ray absorption spectroscopy (XAS) and magnetic circular dichroism (XMCD) techniques, which show that the C $2p_z$ orbitals of the SLG are magnetically polarized due to the hybridization with the valence-band states of the YIG and Py substrates. With this investigation we shed light on the phenomenon of the induced magnetization in the carbon atoms of graphene in contact with magnetic materials and show graphene as a promising material for basic and applied investigation of spintronics phenomena.

## ACKNOWLEDGMENTS

The authors thank Laboratório Nacional de Luz Síncrotron (LNLS) for providing the beam time (Proposal No. 20160219, PGM beamline). The authors would also like to thank Pedro H. R. Gonçalves for the measurement of the spatial drift in the STM/STS results. This research was supported by Conselho Nacional de Desenvolvimento Científico e Tecnológico (CNPq); Coordenação de Aperfeiçoamento de Pessoal de Nível Superior (CAPES), Finance Code 001; Financiadora de Estudos e Projetos (FINEP); INCT de Nanocarbono; Fundação de Amparo à Ciência e Tecnologia do Estado de Pernambuco (FACEPE); Fundação Arthur Bernardes (Funarbe); Fundação de Amparo à Pesquisa do Estado de Minas Gerais (FAPEMIG) - Rede de Pesquisa em Materiais 2D and Rede de Nanomagnetismo.

## APPENDIX A: CONDITIONS FOR GROWTH AND TRANSFERRING OF GRAPHENE

Sample A (YIG/SLG) is prepared in the following way. Graphene is grown on Cu foils inside a CVD chamber at 1000 °C with a mixture of $CH_4$ (33% volume) and $H_2$ (66% volume) at 330 mTorr for 2.5 hours. A 120-nm-thick layer of PMMA is spun on top of the graphene/Cu surface and Cu is then etched away [63,64]. The PMMA/graphene structure is then transferred onto the YIG film, with lateral dimensions of $2.5 \times 8.0$ mm$^2$. Finally, the PMMA is removed and the sample receives two silver paint contacts as illustrated in Fig. 1(a). Figure 8 shows all the steps involving the transfer of graphene. In the case of sample B (Si/$SiO_2$/SLG/Py) the graphene is transferred onto Si/$SiO_2$ substrate with lateral dimensions of $1.5 \times 3.0$ mm$^2$, by the same steps of the previous systematics. After this process is deposited a rectangle of Py film with a thickness of 20 nm at the midpart of graphene,

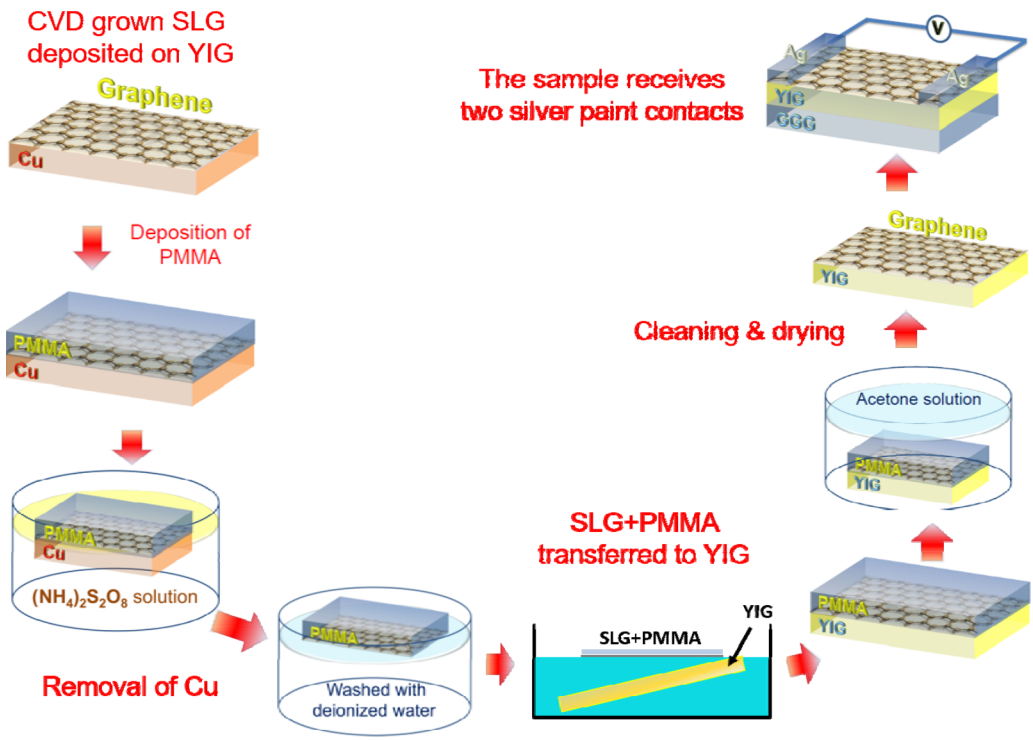


FIG. 8. The sequence of steps made in order to insure the best transference of the single-layer graphene to YIG. Using a similar process, the SLG is transferred to $Si/SiO_2$.

using a $1.5 \times 2.0$ mm$^2$ shadow mask, as seen in Fig. 6(a). Lastly, two silver paint contacts are made on the edges of graphene.

## APPENDIX B: X-RAY ABSORPTION AND MAGNETIC CIRCULAR DICHROISM OF THE PY/SLG SAMPLE

Figure 9(a) shows carbon $K$ edge x-ray absorption spectra acquired with linear vertical polarization of the electric field for sample Py/SLG. Similarly to the results obtained for sample YIG/SLG (main text), the angular dependence of the XAS line shape confirms that the $\pi^*$ unoccupied states (feature around 285 eV, C $1s \rightarrow \pi^*$ transition) are aligned out-of-plane. This result also corroborates the good quality of the SLG transferred to Py thin film. Figure 9(b) shows XMCD asymmetry spectra measured at both Ni $L_{3,2}$ and carbon $K$ edges. The Ni spectrum is representative of the Py layer and characteristic of the metallic environment of this material, while the C spectrum is somehow similar to that of the YIG/SLG, presenting a remarkable asymmetry around the feature related to the $\pi^*$ unoccupied states. This result is also in accordance with previous work for Ni(111)/graphene

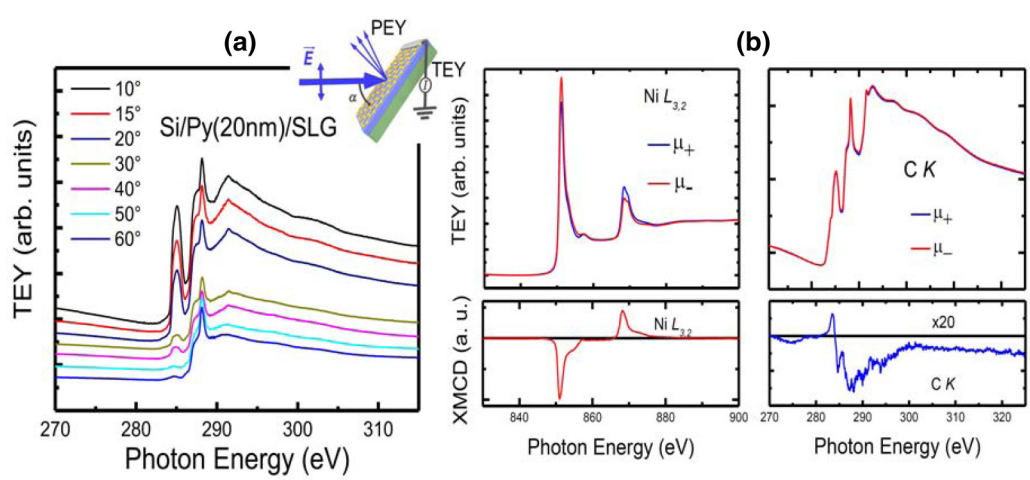


FIG. 9. (a) XAS spectra of Py/graphene measured at $\alpha = 15°$. (b) XAS spectra acquired around the Ni $L_{3,2}$ (left) and C $K$ (right) edges, for both right- and left-handed circular polarizations of the light, under an applied magnetic field of 300 Oe and at an incidence angle of 15°. The bottom of the figure presents the XMCD asymmetries.

[69,70], suggesting that the C $2p_z$ orbitals of the SLG are magnetically polarized due to the hybridization with the valence-band states of the adjacent Py layer.

## APPENDIX C: ADDITIONAL COMMENTS ON XMCD MEASUREMENTS

The tiny dichroism detected at the carbon *K* edge of our samples is very close to the detection limit of the experiment mainly due to instrumental and normalization artifacts. It is important to cite three main sources contributing to the detection limit of the experiment estimated to be around 1%–1.5% of the intensity at the absorption edge: (1) the fact that the spectra were acquired at an undulator beamline of a second-generation synchrotron [UVX accelerator of the Brazilian Synchrotron Light Laboratory (LNLS)] that may present a small asymmetry between the circular polarization for two opposite handednesses; (2) carbon contamination on the surface of the beamline mirrors, a common problem of soft x-ray beamlines; and (3) the possible presence of PMMA on the sample surface (residue of the graphene transferring process). More specifically, items 2 and 3 contribute to make the data very hard to be normalized and background-subtracted as well as to the measured line shape of the XMCD difference spectra presenting some artifacts. In this sense, as the carbon *K* edge spectra of the mirror's contamination present their main features around 280–283 eV, the background subtraction and normalization of the pre-edge of our data are very difficult and we cannot guarantee that the change of sign at the pre-edge is real. Similar problems of the difference spectra line shape are observed around 287–292 eV due to the residue of PMMA on the sample surface. Finally, the small dichroism at the post-edge is below the detection limit of the experiment and can be due to the undulator asymmetry mentioned in item 1, which also may mask the dichroism of any "nonmagnetic" region of the spectrum.

In Fig. 10 we show two spectra (sample YIG/graphene) in order to demonstrate the aforementioned problems: (in red) the raw circular dichroism asymmetry given by the difference between two spectra acquired with opposite handednesses of the circular polarization while keeping the magnetic field fixed, i.e., before carrying out the subtraction of the difference spectra acquired with opposite field to cancel the contribution of the natural circular dichroism as discussed in the main text; and (in black) the difference between two consecutive spectra acquired with both the same polarization and magnetic field, i.e., in the very same conditions. In other words, the curve in black, which we call residue, is representative of the dependence of the detection limit of the experiment on the energy along the carbon *K* absorption edge. Each curve in Fig. 10 is a summation over eight spectra in order to improve statistics, and the curves are evaluated with the same data set in order to get a high confidence of the estimation of the detection limits of the experiment for each sample/condition. It can be noticed that the higher amplitudes of the residue are just below the $\pi^*$ peak and around the PMMA region of the spectra. Besides, the detection limit on the post edge is below the dichroism detected in our samples. Nevertheless, we point out that the peak of the difference spectra at 285 eV is around the $\pi^*$ region of the spectrum and is considerably over

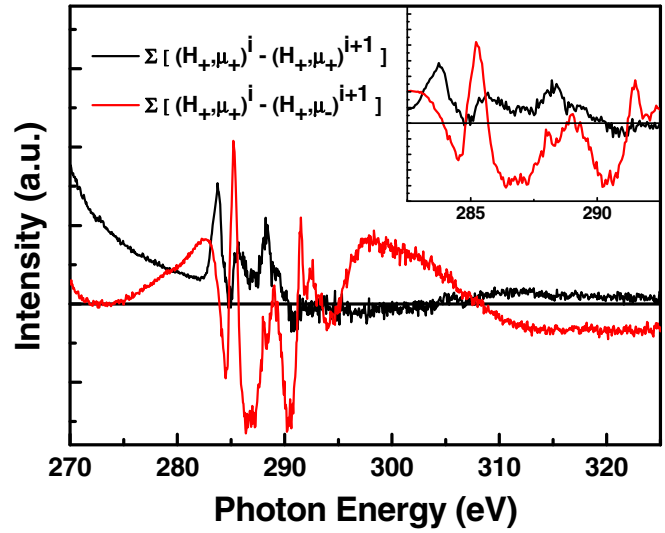


FIG. 10. XMCD spectra of the sample YIG/graphene. In red: Difference between two spectra acquired with opposite handedness of the circular polarization while keeping the magnetic field fixed, i.e., the raw circular dichroism asymmetry. In black: Difference between two consecutive spectra acquired with both same polarization and magnetic field, i.e., in the very same conditions.

the detection limit. After taking the average of the circular dichroism obtained with two opposite-direction magnetic fields, as presented in Fig. 4 of the main text, the magnitude of the XMCD asymmetry agrees quantitatively with Refs. [69,70]. This result suggests that the claimed induced magnetic moment in the graphene layer is due to the hybridization with the valence-band states of the YIG substrate.

## APPENDIX D: EDX SPECTRUM OF GRAPHENE GROWN BY CVD

The energy-dispersive x-ray (EDX) spectrum of SLG by CVD onto the YIG film can be seen in Fig. 11(a). The EDX spectrum taken from an arbitrary region of the sample shows the presence only of yttrium (Y), iron (Fe), oxygen (O) of the YIG film, and carbon (C) of SLG. Different samples were prepared, in order to confirm the results of the EDX measurements. In Fig. 11(b), the samples for EDX measurements are prepared on standard transmission electron

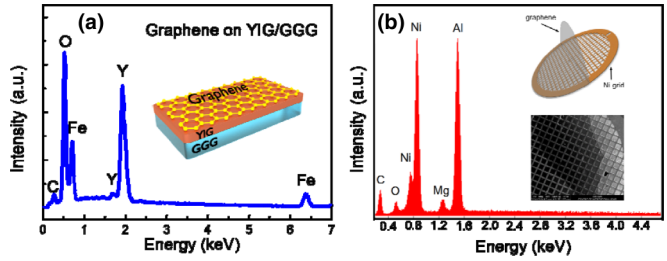


FIG. 11. (a) EDX spectrum from an arbitrary region in the sample of GGG/YIG/graphene. (b) The EDX spectrum of SLG grown by CVD onto the nickel grids. The additional peaks of the Ni, Al, and Mg in the EDX spectrum are due to the presence of Ni TEM grids and the stub (compound of Al and Mg).

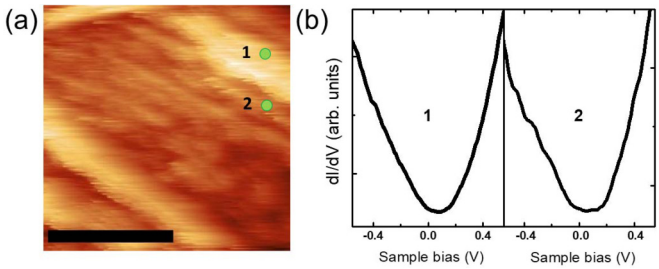


FIG. 12. (a) STM topography image of graphene on YIG. (b) STS spectra acquired at points labeled as 1 and 2 shown in (a). Scale bar is 100 nm.

microscope (TEM) nickel grids and are hence suspended graphene samples (as shown at the top of the insert). The image of the Ni-grid/SLG sample analyzed by electron microscopy is shown at the bottom of the inset of Fig. 11(b). The EDX spectrum shows the presence only of oxygen (O) and carbon (C) of SLG. The additional peaks of the Ni, Al, and Mg in the EDX spectrum are due to the presence of Ni TEM grids and the stub (compound of Al and Mg) that served as a support on which the graphene samples are prepared for analysis. This result confirms that there are no visible traces of Cu adatoms on the graphene layer.

## APPENDIX E: ADDITIONAL COMMENTS ON STM/STS EXPERIMENTS

As is generally known, STS measurements are very sensitive to the tip condition, so in order avoid misinterpretation of our experimental data some procedures were stablished. It is important to mention, for instance, that the tip was prepared and tested using graphite substrates (HOPG). Besides, good-topography STM images and reliable STS spectra were acquired before the measurements of graphene on YIG. In order to clarify the results presented in the paper additional measurements are presented in Fig. 12.

Figure 12(a) shows a region of the graphene on the YIG sample studied in this work. STS spectra, shown in Fig. 12(b), were measured at the points labeled as "1" and "2" shown in Fig. 12(a). STS spectra shown in this figure were measured with the same tip and in the same conditions. As depicted in Fig. 12(b) the STS spectrum labeled as "1" presents a V-shaped behavior typical of graphene systems that do not highly interact with the substrate. On the other hand, for the STS labeled as "2" one observes small deviations from the V-shaped; in particular, the STS spectrum resembles more a U-shaped behavior, which may indicate more interaction with the substrate for this region. Thus, these measurements support our interpretation of the STS results of Fig. 3 of the main text. It is also well known from a number of studies that graphene, as well as other 2D materials, is extremely sensitive to interactions with the substrate. These interactions may modify its electronic properties, and consequently its electronic density of states, in many different ways [82–85].

Finally, it is important to emphasize that for all the STS measurements presented in this work we have to take into account the reproducibility of the results; i.e., STS curves that presented atypical behaviors were not considered or used for any physical interpretation of our results. Our results

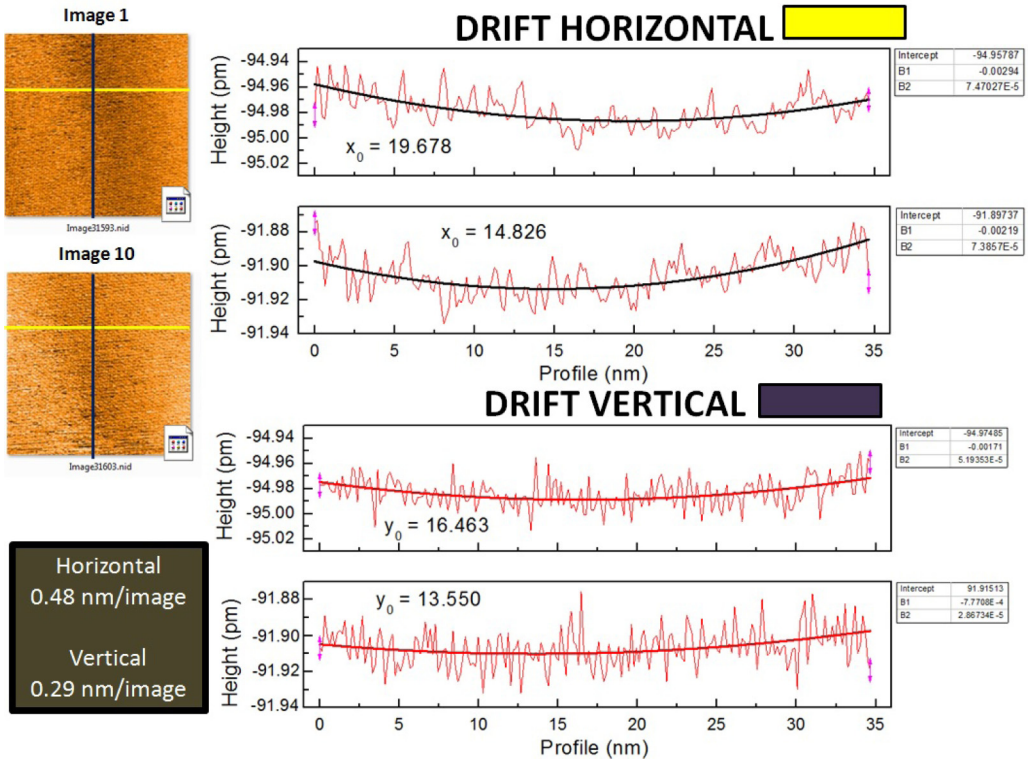


FIG. 13. Experimental determination of spatial drift for STM/STS measurements at room temperature.

were corrected for spatial drift and are reproducible within ∼0.5 nm. In Fig. 13 we presented the experimental determination of spatial drift for our STM/STS measurements at room temperature. In the figure it is possible to verify that the stability of our measurements is better than 0.3 nm per image (vertical direction) and 0.5 nm per image (horizontal).


[1] I. Žutić, J. Fabian, and S. Das Sarma, Spintronics: Fundamentals and applications, Rev. Mod. Phys. **76**, 323 (2004).

[2] A. Hoffmann and S. D. Bader, Opportunities at the Frontiers of Spintronics, Phys. Rev. Appl. **4**, 047001 (2015).

[3] M. I. D'yakonov and V. I. Perel', Possibility of orienting electron spins with current, ZhETF Pis. Red. **13**, 657 (1971) [JETP Lett. **13**, 467 (1971)].

[4] J. E. Hirsch, Spin Hall Effect, Phys. Rev. Lett. **83**, 1834 (1999).

[5] S. Zhang, Spin Hall Effect in the Presence of Spin Diffusion, Phys. Rev. Lett. **85**, 393 (2000).

[6] Y. Tserkovnyak, A. Brataas, and G. E. W. Bauer, Enhanced Gilbert Damping in Thin Ferromagnetic Films, Phys. Rev. Lett. **88**, 117601 (2002).

[7] Y. K. Kato, R. C. Myers, A. C. Gossard, and D. D. Awschalom, Observation of the spin Hall effect in semiconductors, Science **306**, 1910 (2004).

[8] J. Wunderlich, B. Kaestner, J. Sinova, and T. Jungwirth, Experimental Observation of the Spin-Hall Effect in a Two-Dimensional Spin-Orbit Coupled Semiconductor System, Phys. Rev. Lett. **94**, 047204 (2005).

[9] A. Azevedo, L. H. Vilela Leão, R. L. Rodriguez-Suarez, A. B. Oliveira, and S. M. Rezende, dc effect in ferromagnetic resonance: Evidence of the spin-pumping effect? J. Appl. Phys. **97**, 10C715 (2005).

[10] E. Saitoh, M. Ueda, H. Miyajima, and G. Tatara, Conversion of spin current into charge current at room temperature: Inverse spin-Hall effect, Appl. Phys. Lett. **88**, 182509 (2006).

[11] S. O. Valenzuela and M. Tinkham, Direct electronic measurement of the spin Hall effect, Nature (London) **442**, 176 (2006).

[12] L. J. Cornelissen, J. Liu, R. A. Duine, J. Ben Youssef, and B. J. van Wees, Long-distance transport of magnon spin information in a magnetic insulator at room temperature, Nat. Phys. **11**, 1022 (2015).

[13] H. Wang, C. Du, P. C. Hammel, and F. Yang, Spin transport in antiferromagnetic insulators mediated by magnetic correlations, Phys. Rev. B **91**, 220410(R) (2015).

[14] J. Holanda, D. S. Maior, O. Alves Santos, L. H. Vilela-Leão, J. B. S. Mendes, A. Azevedo, R. L. Rodríguez-Suárez, and S. M. Rezende, Spin Seebeck effect in the antiferromagnet nickel oxide at room temperature, Appl. Phys. Lett. **111**, 172405 (2017).

[15] K. Ando, S. Watanabe, S. Mooser, E. Saitoh, and H. Sirringhaus, Solution-processed organic spin-charge converter, Nat. Mater. **12**, 622 (2013).

[16] S. W. Jiang, S. Liu, P. Wang, Z. Z. Luan, X. D. Tao, H. F. Ding, and D. Wu, Exchange-Dominated Pure Spin Current Transport in $Alq_3$ Molecules, Phys. Rev. Lett. **115**, 086601 (2015).

[17] J. B. S. Mendes, O. Alves Santos, J. P. Gomes, H. S. Assis, J. F. Felix, R. L. Rodríguez-Suárez, S. M. Rezende, and A. Azevedo, Efficient spin transport through polyaniline, Phys. Rev. B **95**, 014413 (2017).

[18] A. Azevedo, L. H. Vilela-Leão, R. L. Rodríguez-Suárez, A. F. Lacerda Santos, and S. M. Rezende, Spin pumping and anisotropic magnetoresistance voltages in magnetic bilayers: Theory and experiment, Phys. Rev. B **83**, 144402 (2011).

[19] A. Hoffmann, Spin Hall effects in metals, IEEE Trans. Magn. **49**, 5172 (2013).

[20] J. B. S. Mendes, R. O. Cunha, O. Alves Santos, P. R. T. Ribeiro, F. L. A. Machado, R. L. Rodríguez-Suárez, A. Azevedo, and S. M. Rezende, Large inverse spin Hall effect in the antiferromagnetic metal $Ir_{20}Mn_{80}$, Phys. Rev. B **89**, 140406(R) (2014).

[21] J. Sinova, S. O. Valenzuela, J. Wunderlich, C. H. Back, and T. Jungwirth, Spin Hall effects, Rev. Mod. Phys. **87**, 1213 (2015).

[22] K. Ando, S. Takahashi, J. Ieda, H. Kurebayashi, T. Trypiniotis, C. H. W. Barnes, S. Maekawa, and E. Saitoh, Electrically tunable spin injector free from the impedance mismatch problem, Nat. Mater. **10**, 655 (2011).

[23] O. Alves-Santos, E. F. Silva, M. Gamino, R. O. Cunha, J. B. S. Mendes, R. L. Rodríguez-Suárez, S. M. Rezende, and A. Azevedo, Giant spin-charge conversion driven by nanoscopic particles of Ag in Pt, Phys. Rev. B **96**, 060408(R) (2017).

[24] K. Ando and E. Saitoh, Observation of the inverse spin Hall effect in silicon, Nat. Commun. **3**, 629 (2012).

[25] E. Shikoh, K. Ando, K. Kubo, E. Saitoh, T. Shinjo, and M. Shiraishi, Spin-Pump-Induced Spin Transport in *p*-Type Si at Room Temperature, Phys. Rev. Lett. **110**, 127201 (2013).

[26] S. Dushenko, M. Koike, Y. Ando, T. Shinjo, M. Myronov, and M. Shiraishi, Experimental Demonstration of Room-Temperature Spin Transport in *n*-Type Germanium Epilayers, Phys. Rev. Lett. **114**, 196602 (2015).

[27] F. Bottegoni, C. Zucchetti, S. Dal Conte, J. Frigerio, E. Carpene, C. Vergnaud, M. Jamet, G. Isella, F. Ciccacci, G. Cerullo, and M. Finazzi, Voltage over a Large Length Scale in Bulk Germanium, Phys. Rev. Lett. **118**, 167402 (2017).

[28] J. B. S. Mendes, S. L. A. Mello, O. Alves Santos, R. O. Cunha, R. L. Rodríguez-Suárez, A. Azevedo, and S. M. Rezende, Inverse spin Hall effect in the semiconductor (Ga,Mn)As at room temperature, Phys. Rev. B **95**, 214405 (2017).

[29] W. Rippard, M. Pufall, S. Kaka, S. Russek, and T. Silva, Direct-Current Induced Dynamics in $Co_{90}Fe_{10}/Ni_{80}Fe_{20}$ Point Contacts, Phys. Rev. Lett. **92**, 027201 (2004).

[30] I. N. Krivorotov, N. C. Emley, J. C. Sankey, S. I. Kiselev, D. C. Ralph, and R. A. Buhrman, Time-domain measurements of nanomagnet dynamics driven by spin-transfer torques, Science **307**, 228 (2005).

[31] S. M. Rezende, F. M. de Aguiar, and A. Azevedo, Spin-Wave Theory for the Dynamics Induced by Direct Currents in Magnetic Multilayers, Phys. Rev. Lett. **94**, 037202 (2005).

[32] L. Liu, C.-F. Pai, Y. Li, H. W. Tseng, D. C. Ralph, and R. A. Buhrman, Spin-torque switching with the giant spin Hall effect of tantalum, Science **336**, 555 (2012).

[33] S. Urazhdin, V. E. Demidov, H. Ulrichs, T. Kendziorczyk, T. Kuhn, J. Leuthold, G. Wilde, and S. O. Demokritov, Nanomagnonic devices based on the spin-transfer torque, Nat. Nanotechnol. **9**, 509 (2014).

[34] J. C. R. Sánchez, L. Vila, G. Desfonds, S. Gambarelli, J. P. Attané, J. M. De Teresa, C. Magén, and A. Fert, Spin-to-charge conversion using Rashba coupling at the interface between nonmagnetic materials, Nat. Commun. **4**, 2944 (2013).

[35] A. Soumyanarayanan, N. Reyren, A. Fert, and C. Panagopoulos, Emergent phenomena induced by spin-orbit coupling at surfaces and interfaces, Nature (London) **539**, 509 (2016).

[36] A. Manchon, H. C. Koo, J. Nitta, S. M. Frolov, and R. A. Duine, New perspectives for Rashba spin-orbit coupling, Nat. Mater. **14**, 871 (2015).

[37] K. Shen, G. Vignale, and R. Raimondi, Microscopic Theory of the Inverse Edelstein Effect, Phys. Rev. Lett. **112**, 096601 (2014).

[38] J. B. S. Mendes, O. Alves Santos, L. M. Meireles, R. G. Lacerda, L. H. Vilela-Leão, F. L. A. Machado, R. L. Rodríguez-Suárez, A. Azevedo, and S. M. Rezende, Spin-Current to Charge-Current Conversion and Magnetoresistance in a Hybrid Structure of Graphene and Yttrium Iron Garnet, Phys. Rev. Lett. **115**, 226601 (2015).

[39] H. Wang, J. Kally, J. S. Lee, T. Liu, H. Chang, D. R. Hickey, K. A. Mkhoyan, M. Wu, A. Richardella, and N. Samarth, Surface-State-Dominated Spin-Charge Current Conversion in Topological-Insulator–Ferromagnetic-Insulator Heterostructures, Phys. Rev. Lett. **117**, 076601 (2016).

[40] J. B. S. Mendes, O. Alves Santos, J. Holanda, R. P. Loreto, C. I. L. de Araujo, C.-Z. Chang, J. S. Moodera, A. Azevedo, and S. M. Rezende, Dirac-surface-state-dominated spin to charge current conversion in the topological insulator $(Bi_{0.22}Sb_{0.78})_2Te_3$ films at room temperature, Phys. Rev. B **96**, 180415(R) (2017).

[41] J. B. S. Mendes, A. Aparecido-Ferreira, J. Holanda, A. Azevedo, and S. M. Rezende, Efficient spin to charge current conversion in the 2D semiconductor $MoS_2$ by spin pumping from yttrium iron garnet, Appl. Phys. Lett. **112**, 242407 (2018).

[42] K. S. Novoselov, A. K. Geim, S. V. Morozov, D. Jiang, Y. Zhang, S. V. Dubonos, I. V. Grigorieva, and A. A. Firsov, Electric field effect in atomically thin carbon films, Science **306**, 666 (2004).

[43] K. S. Novoselov, A. K. Geim, S. V. Morozov, D. Jiang, M. I. Katsnelson, I. V. Grigorieva, S. V. Dubonos, and A. A. Firsov, Two-dimensional gas of massless Dirac fermions in graphene, Nature (London) **438**, 197 (2005).

[44] A. H. Castro Neto, F. Guinea, N. M. R. Peres, K. S. Novoselov, and A. K. Geim, The electronic properties of graphene, Rev. Mod. Phys. **81**, 109 (2009).

[45] A. Ferreira, T. G. Rappoport, M. A. Cazalilla, and A. H. Castro Neto, Extrinsic Spin Hall Effect Induced by Resonant Skew Scattering in Graphene, Phys. Rev. Lett. **112**, 066601 (2014).

[46] J. Balakrishnan, G. K. W. Koon, A. Avsar, Y. Ho, J. H. Lee, M. Jaiswal, S.-J. Baeck, J.-H. Ahn, A. Ferreira, M. A. Cazalilla, A. H. C. Neto, and B. Özyilmaz, Giant spin Hall effect in graphene grown by chemical vapour deposition, Nat. Commun. **5**, 4748 (2014).

[47] D. Bercioux, D. F. Urban, F. Romeo, and R. Citro, Rashba spin-orbit-interaction-based quantum pump in graphene, Appl. Phys. Lett. **101**, 122405 (2012).

[48] Q. Zhang, Z. Lin, and K. S. Chan, Pure spin current generation in monolayer graphene by quantum pumping, J. Phys.: Condens. Matter **24**, 075302 (2012).

[49] H. X. Yang, A. Hallal, D. Terrade, X. Waintal, S. Roche, and M. Chshiev, Proximity Effects Induced in Graphene by Magnetic Insulators: First-Principles Calculations on Spin Filtering and Exchange-Splitting Gaps, Phys. Rev. Lett. **110**, 046603 (2013).

[50] J. Lee and J. Fabian, Magnetotransport signatures of the proximity exchange and spin-orbit couplings in graphene, Phys. Rev. B **94**, 195401 (2016).

[51] Z. Tang, E. Shikoh, H. Ago, K. Kawahara, Y. Ando, T. Shinjo, and M. Shiraishi, Dynamically generated pure spin current in single-layer graphene, Phys. Rev. B **87**, 140401(R) (2013).

[52] S. Singh, A. Ahmadi, C. T. Cherian, E. R. Mucciolo, E. del Barco, and B. Özyilmaz, Dynamical spin injection at a quasi-one-dimensional ferromagnet-graphene interface, Appl. Phys. Lett. **106**, 032411 (2015).

[53] J. G. G. S. Ramos, T. C. Vasconcelos, and A. L. R. Barbosa, Spin-to-charge conversion in 2D electron gas and single-layer graphene devices, J. Appl. Phys. **123**, 034304 (2018).

[54] T. S. Ghiasi, J. Ingla-Aynés, A. A. Kaverzin, and B. J. van Wees, Large proximity-induced spin lifetime anisotropy in transition-metal dichalcogenide/graphene heterostructures, Nano Lett. **17**, 7528 (2017).

[55] L. A. Benítez, J. F. Sierra, W. S. Torres, A. Arrighi, F. Bonell, M. V Costache, and S. O. Valenzuela, Strongly anisotropic spin relaxation in graphene–transition metal dichalcogenide heterostructures at room temperature, Nat. Phys. **14**, 303 (2018).

[56] J. H. Garcia, M. Vila, A. W. Cummings, and S. Roche, Spin transport in graphene/transition metal dichalcogenide heterostructures, Chem. Soc. Rev. **47**, 3359 (2018).

[57] C. K. Safeer, J. Ingla-Aynés, F. Herling, J. H. Garcia, M. Vila, N. Ontoso, M. R. Calvo, S. Roche, L. E. Hueso, and F. Casanova, Room-temperature spin Hall effect in graphene/$MoS_2$ van der Waals heterostructures, Nano Lett. **19**, 1074 (2019).

[58] Z. Wang, C. Tang, R. Sachs, Y. Barlas, and J. Shi, Proximity-Induced Ferromagnetism in Graphene Revealed by the Anomalous Hall Effect, Phys. Rev. Lett. **114**, 016603 (2015).

[59] S. Dushenko, H. Ago, K. Kawahara, T. Tsuda, S. Kuwabata, T. Takenobu, T. Shinjo, Y. Ando, and M. Shiraishi, Gate-Tunable Spin-Charge Conversion and the Role of Spin-Orbit Interaction in Graphene, Phys. Rev. Lett. **116**, 166102 (2016).

[60] J. C. Leutenantsmeyer, A. A. Kaverzin, M. Wojtaszek, and B. J. van Wees, Proximity induced room temperature ferromagnetism in graphene probed with spin currents, 2D Mater. **4**, 014001 (2016).

[61] S. Sakai, S. Majumdar, Z. I. Popov, P. V. Avramov, S. Entani, Y. Hasegawa, Y. Yamada, H. Huhtinen, H. Naramoto, P. B. Sorokin, and Y. Yamauchi, Proximity-induced spin polarization of graphene in contact with half-metallic manganite, ACS Nano **10**, 7532 (2016).

[62] M. Evelt, H. Ochoa, O. Dzyapko, V. E. Demidov, A. Yurgens, J. Sun, Y. Tserkovnyak, V. Bessonov, A. B. Rinkevich, and S. O. Demokritov, Chiral charge pumping in graphene deposited on a magnetic insulator, Phys. Rev. B **95**, 024408 (2017).

[63] I. Silvestre, A. W. Barnard, S. P. Roberts, P. L. McEuen, and R. G. Lacerda, Folded graphene nanochannels via pulsed patterning of graphene, Appl. Phys. Lett. **106**, 153105 (2015).

[64] I. D. Barcelos, L. G. Moura, R. G. Lacerda, and A. Malachias, Observation of strain-free rolled-up CVD graphene single layers: Toward unstrained heterostructures, Nano Lett. **14**, 3919 (2014).

[65] M. Golor, S. Wessel, and M. J. Schmidt, Quantum Nature of Edge Magnetism in Graphene, Phys. Rev. Lett. **112**, 046601 (2014).

[66] C. J. Chen, *Introduction to Scanning Tunneling Microscopy* (Oxford University Press, New York, 1993).

[67] C.-J. Kim, A. Sánchez-Castillo, Z. Ziegler, Y. Ogawa, C. Noguez, and J. Park, Chiral atomically thin films, Nat. Nanotechnol. **11**, 520 (2016).

[68] J. Stöhr, *NEXAFS Spectroscopy* (Springer, Berlin, 1992).

[69] Y. S. Dedkov and M. Fonin, Electronic and magnetic properties of the graphene-ferromagnet interface, New J. Phys. **12**, 125004 (2010).

[70] Y. S. Dedkov, M. Sicot, and M. Fonin, X-ray absorption and magnetic circular dichroism of graphene/Ni(111), J. Appl. Phys. **107**, 09E121 (2010).

[71] B. B. Krichevtsov, S. V. Gastev, S. M. Suturin, V. V. Fedorov, A. M. Korovin, V. E. Bursian, A. G. Banshchikov, M. P. Volkov, M. Tabuchi, and N. S. Sokolov, Magnetization reversal in YIG/GGG(111) nanoheterostructures grown by laser molecular beam epitaxy, Sci. Technol. Adv. Mater. **18**, 351 (2017).

[72] H.-C. Mertins, S. Valencia, W. Gudat, P. M. Oppeneer, O. Zaharko, and H. Grimmer, Direct observation of local ferromagnetism on carbon in C/Fe multilayers, Europhys. Lett. **66**, 743 (2004).

[73] W. Q. Liu, W. Y. Wang, J. J. Wang, F. Q. Wang, C. Lu, F. Jin, A. Zhang, Q. M. Zhang, G. van der Laan, Y. B. Xu, Q. X. Li, and R. Zhang, Atomic-scale interfacial magnetism in Fe/graphene heterojunction, Sci. Rep. **5**, 11911 (2015).

[74] O. Céspedes, M. S. Ferreira, S. Sanvito, M. Kociak, and J. M. D. Coey, Contact induced magnetism in carbon nanotubes, J. Phys.: Condens. Matter **16**, L155 (2004).

[75] M. Buscema, M. Barkelid, V. Zwiller, H. S. J. Van Der Zant, G. A. Steele, and A. Castellanos-Gomez, Large and tunable photothermoelectric effect in single-layer $MoS_2$, Nano Lett. **13**, 358 (2013).

[76] H. Emoto, Y. Ando, G. Eguchi, R. Ohshima, E. Shikoh, Y. Fuseya, T. Shinjo, and M. Shiraishi, Transport and spin conversion of multicarriers in semimetal bismuth, Phys. Rev. B **93**, 174428 (2016).

[77] Yu. A. Bychkov and E. I. Rashba, Properties of a 2D electron gas with lifted spectral degeneracy, Pis'ma Zh. Eksp. Teor. Fiz. **39**, 66 (1984) [JETP Lett. **39**, 78 (1984)].

[78] R. O. Cunha, J. Holanda, L. H. Vilela-Leão, A. Azevedo, R. L. Rodríguez-Suárez, and S. M. Rezende, Nonlinear dynamics of three-magnon process driven by ferromagnetic resonance in yttrium iron garnet, Appl. Phys. Lett. **106**, 192403 (2015).

[79] O. Dzyapko, H. Kurebayashi, V. E. Demidov, M. Evelt, A. J. Ferguson, and S. O. Demokritov, Effect of the magnetic film thickness on the enhancement of the spin current by multi-magnon processes, Appl. Phys. Lett. **102**, 252409 (2013).

[80] S. Maekawa, H. Adachi, K. Uchida, J. Ieda, and E. Saitoh, Spin current: Experimental and theoretical aspects, J. Phys. Soc. Jpn. **82**, 102002 (2013).

[81] O. Mosendz, J. E. Pearson, F. Y. Fradin, G. E. W. Bauer, S. D. Bader, and A. Hoffmann, Quantifying Spin Hall Angles from Spin Pumping: Experiments and Theory, Phys. Rev. Lett. **104**, 046601 (2010).

[82] V. W. Brar, Y. Zhang, Y. Yayon, T. Ohta, J. L. McChesney, A. Bostwick, E. Rotenberg, K. Horn, and M. F. Crommie, Scanning tunneling spectroscopy of inhomogeneous electronic structure in monolayer and bilayer graphene on SiC, Appl. Phys. Lett. **91**, 122102 (2007).

[83] E. Sutter, D. P. Acharya, J. T. Sadowski, and P. Sutter, Scanning tunneling microscopy on epitaxial bilayer graphene on ruthenium (0001), Appl. Phys. Lett. **94**, 133101 (2009).

[84] L. Gao, J. R. Guest, and N. P. Guisinger, Epitaxial graphene on Cu(111), Nano Lett. **10**, 3512 (2010).

[85] I. Jeon, H. Yang, S.-H. Lee, J. Heo, D. H. Seo, J. Shin, U.-I. Chung, Z. G. Kim, H.-J. Chung, and S. Seo, Passivation of metal surface states: Microscopic origin for uniform monolayer graphene by low temperature chemical vapor deposition, ACS Nano **5**, 1915 (2011).